Plasmonics (2019) 14:1801–1815
https://doi.org/10.1007/s11468-019-00976-z

All Ceramic-Based Metal-Free Ultra-broadband Perfect Absorber

Mahmut Can Soydan[1,2] · Amir Ghobadi[1,2] · Deniz Umut Yildirim[1,2] · Vakur Behcet Erturk[2] · Ekmel Ozbay[1,2,3,4]

Received: 17 February 2019 / Accepted: 3 June 2019 / Published online: 19 June 2019

Abstract

In this paper, we scrutinize unprecedented potential of transition metal carbides (TMCs) and nitrides (TMNs) for realization of light perfect absorption in an ultra-broad frequency range encompassing all of the visible (Vis) and near infrared (NIR) regions. For this purpose, two different configurations which are planar and trapezoidal array are employed. To gain insight on the condition for light perfect absorption, a systematic modeling approach based on transfer matrix method (TMM) is firstly utilized. Our modeling findings prove that the permittivity data of these TMCs and TMNs are closely matched with the ideal data. Thus, they can have stronger and broader absorption behavior compared to metals. Besides, these ceramic materials are preferred to metals due to the fact that they have better thermal properties and higher durability against erosion and oxidation than metals. This could provide the opportunity for design of highly efficient light harvesting systems with long-term stability. Numerical simulations are conducted to optimize the device optical performance for each of the proposed carbides and nitrides. Our findings reveal that these ceramic coatings have the broadest absorption response compared to all lossy and plasmonic metals. In planar configuration, titanium carbide (TiC) has the largest absorption bandwidth (BW) where an absorption above 0.9 is retained over a broad wavelength range of 405–1495 nm. In trapezoid architecture, vanadium nitride (VN) shows the widest BW covering a range from 300 to 2500 nm. The results of this study can serve as a beacon for the design of future high-performance energy conversion devices including solar vapor generation and thermal photovoltaics where both optical and thermal requirements can be satisfied.

Keywords Metamaterials · Broadband perfect absorber · Metal-free · Transition metal nitrides · Transition metal carbides

Introduction

A high-performance light absorber is one of the most studied topics in nanophotonics, leading to different attempts to devise perfect light absorbers, operating either in narrowband or broadband frequency regimes, by using various materials and structures. Perfect absorbers have a variety of applications in research areas such as sensing [1], spectroscopy [2], photovoltaic [3] and thermal photovoltaic [4], and solar vapor generation as well as photodetection [5]. Metamaterials, with their exceptional properties that cannot be observed in nature, are of great use for the purpose of designing the optimum perfect absorber. One of the most commonly used structure in order to achieve near-unity light absorption is metal-dielectric-metal (MDM) architecture [6–17]. In this structure, dielectric films are sandwiched by a patterned metal film and a flat thick metal layer. The insertion of the dielectric layer between thin metal layers boosts the absorption of the structure by efficiently coupling of incident light into the cavity modes of the MDM design. The bottom metal layer acts as an ideal mirror that reflects all incoming wave back into the cavity, and the top metallic patterned layer includes nanoresonant units to couple the light inside the structure. To improve the bandwidth (BW) of a perfect absorber, different patterning structures such as nanopatches [18–20], nanodiscs [7, 21], or nanorings [22] were developed. These structures can behave as ultra-broadband [12–16] as well as narrowband [11] perfect absorbers, and can carry properties such as polarization

✉ Mahmut Can Soydan
soydan@ee.bilkent.edu.tr

1 NANOTAM-Nanotechnology Research Center, Bilkent University, 06800, Ankara, Turkey

2 Department of Electrical and Electronics Engineering, Bilkent University, 06800, Ankara, Turkey

3 Department of Physics, Bilkent University, 06800, Ankara, Turkey

4 UNAM-Institute of Materials Science and Nanotechnology, Bilkent University, Ankara, Turkey

independence [15–17] and angle tolerance [23] depending on the pattern of the top layer and thickness of the dielectric layer. Although great performances can be attained with these structures, they are large-scale incompatible because electron beam lithography (EBL) is required to fabricate the patterned top layer.

In a recent study, it was theoretically and experimentally demonstrated that the use of planar metal-dielectric (MD) pair multilayer design can provide an ultra-broadband light absorption [24]. Many planar, lithography-free, and high performance designs were developed and fabricated using this configuration [25–27] because it has an obvious advantage of ease of fabrication, and thus, large-scale compatibility. Very recently, our group prepared a perspective on the lithography-free metamaterial perfect absorbers to explore material and architecture requirements and limits for the realization of light perfect absorption in different wavelength regimes [28]. Later, some studies revealed that the light absorption spectrum can be extended using hyperbolic metamaterials (HMMs) [29–34]. A substantial improvement in the absorption BW could be acquired by tapering this multilayer design. The tapered shape enables coupling of the incident photons in a wide-frequency range by gradual matching of the air impedance into the underlying metamaterial configuration [35]. Lei et al. realized an angle-tolerant, polarization-insensitive, and omnidirectional absorber from 200 nm to 3.6 μm using an HMM structure with alternating 20 pairs of aluminum (Al) and germanium (Ge) multilayered films [29]. Besides all these improvements in perfect absorbers, these multilayer designs suffer from multiple depositions and complex processes that limit their applicability for large-scale applications. Moreover, in many applications such as thermal photovoltaic and solar vapor generation, the high operation temperature could deform the layers. A better option for designing such ultra-broadband absorbers is to replace metals with a high-temperature tolerant medium since metals have an inherent lossy nature and exposed to erosion and oxidation under temperature and humidity.

Ceramic materials are the suitable choices to be used instead of metals to improve the performance of the designed structure because ceramics have less lossy nature, a higher melting point compared to noble metals, and more durability against oxidation and corrosion. In recent years, titanium nitride (TiN) has become a promising alternative to metals and has been successfully integrated in metal-free metamaterial designs in some studies [36–42]. Recent reviews also highlighted the tremendous potential of these ceramics in different light-matter interaction applications [43–47]. Taking all of these into account, it is of great importance to design a ceramic-based ultrathin design configuration to realize perfect light absorption in an ultra-broadband wavelength regime where both optical and thermal properties of the metamaterial design will be simultaneously satisfied.

In the present paper, we reveal the high potential of transition metal carbides (TMCs) and nitrides (TMNs) to be used instead of metals in ultra-broadband perfect absorbers making use of their excellent thermal properties (e.g., extremely high melting point) and superior absorption performance compared to metals in any configuration. For this purpose, we propose ultra-broadband near-unity light absorber designs based on TMC (or TMN) in two different configurations: planar and trapezoidal MD pair–based array structure, and compare the performance of the proposed designs with metallic-based corresponding. We use titanium carbide (TiC) and vanadium carbide (VC) as TMC, TiN and vanadium nitride (VN) as TMN, and aluminum oxide (Al_2O_3), silicon dioxide (SiO_2), and titanium dioxide (TiO_2) as the insulator material. Also different lossy metals such as titanium (Ti), platinum (Pt), and nickel (Ni) are used to compare the performance of metallic-based and ceramic-based designs. The paper is organized as follows: In the first part of paper, a systematic modeling approach based on transfer matrix method (TMM) is carried out to reveal compatibility of permittivity data of TMCs and TMNs for broadband perfect absorber designs. Afterwards, by conducting finite-difference time-domain (FDTD) method is employed to find the optimal geometries for each TiC/VC/TiN/VN and Al_2O_3 pairs in planar metal-dielectric-metal-dielectric (MDMD) configuration separately to obtain the broadest attainable absorption spectrum. It is shown that TiC-Al_2O_3 pair offers the best performance among these materials with an absorption BW as wide as 1090 nm covering from 405 to 1495 nm with an average absorption value of 0.95. This BW is not only significantly wider than TiN-based multilayer designs [36, 40], but also larger than that of the highest reported BW for a metal-based MDMD configuration, where a wavelength range of 400–1400 nm was absorbed utilizing the optimal case of a chromium(Cr)-SiO_2 multilayer configuration [48]. Next, trapezoidal array structure is proposed as an option to increase the absorption BW of the design. Geometries of the structure were optimized in a similar fashion for each pair of TMCs/TMNs/metals and Al_2O_3 separately when a 3-MD pair trapezoidal array structure is in use. VN-Al_2O_3 pair offered the strongest absorption profile with an amount above 0.9 in the wavelength range from 300 to 2500 nm, with a BW of 2200 nm, which is much wider than the BW of metallic designs. In addition, possible fabrication inaccuracies are considered, their possible effects are scrutinized and an alternative design is proposed to preserve the same performance for trapezoidal array structure. Considering their optical and thermal properties, TMCs and

TMNs are excellent choices for thermophotovoltaic and solar vapor generation applications where both high optical absorption and long-term durability can be acquired.

Modeling

The schematic illustration of the first proposed multilayer structure is depicted in Fig. 1a. According to this panel, the structure mainly consists of two MD pairs, which are comprised of the same materials, stacked on top of each other. The bottom metal layer is thick enough to act as a perfect mirror that reflects all the light back into the cavity. The bottom insulator layer acts as a spacer between the bottom and middle metal layers in order to create an MDM cavity. The top insulator layer, added onto the MDM cavity, behaves like a broadband antireflective coating to match air impedance to that of an underneath metal layer. In this design, the operational performance of the multilayer is mainly determined by the middle metal layer. The thickness and type of this metal have to be selected in such a way that it should be thin enough to allow light penetration into the cavity and it should be thick enough to trap the light inside of it. For the starting point in designing the multilayer perfect absorber, we first adopted a modeling approach to find the ideal material for the middle layer in which the overall reflection from the MDMD structure is zero. To achieve this goal, the transfer matrix method (TMM) was carried out to find the overall reflection from the design. In this method, we suppose the MDMD structure is bounded with a material of ε_A which is the air in our case. For the transverse magnetic (TM) polarization, considering the H_y as

$$H_y(z) = \begin{cases} A_i e^{ik_A z} + A_r e^{-ik_A z}, & z < 0 \\ D_{11} e^{ik_D z} + D_{12} e^{-ik_D z}, & 0 < z < D_D \\ M_{11} e^{ik_M (z-D_D)} + M_{11} e^{-ik_M (z-D_D)}, & D_D < z < D_D + D_M \\ D_{21} e^{ik_D [z-(D_D+D_M)]} + D_{22} e^{-ik_D [z-(D_D+D_M)]}, & D_D + D_M < z < 2D_D + D_M \\ M_{21} e^{ik_M [z-(2D_D+D_R)]} + M_{22} e^{-ik_M [z-(2D_D+D_R)]}, & 2D_D + D_M < z < 2D_D + D_M + D_R \\ A_t e^{ik_A [z-(2D_D+D_R)]}, & z > 2D_D + D_M + D_R \end{cases} \quad (1)$$

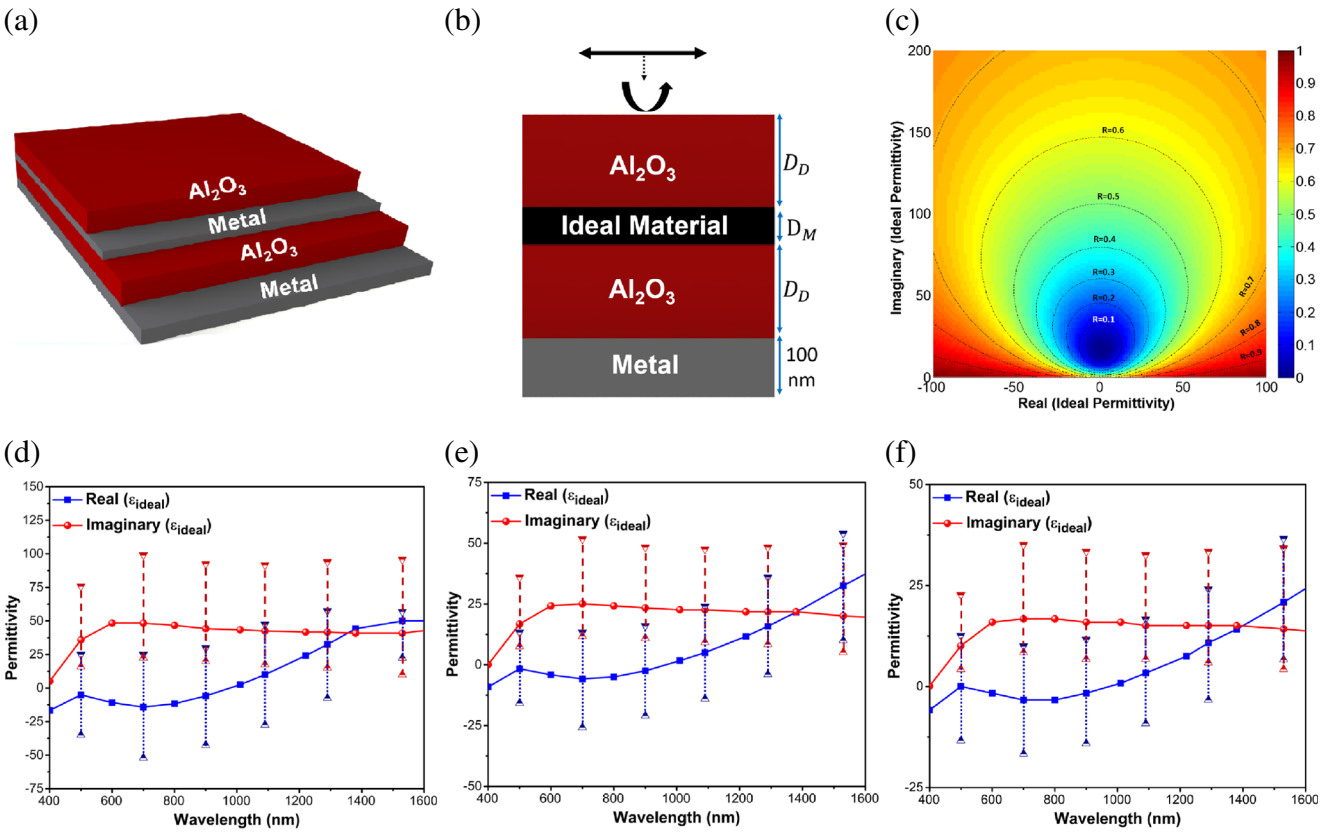

Fig. 1 Designed structure and ideal material. Schematic illustration of the proposed **a** multilayer structure and **b** setup to obtain ideal middle layer. Part **c** depicts the contour plot for reflection value as a function of real and imaginary parts of permittivity for a 10-nm ideal middle layer at the wavelength of 1000 nm. Zero reflection point (ZRP) values and tolerable region for $R < 0.1$ for different middle layer thickness of **d** 5 nm, **e** 10 nm, and **f** 15 nm are also displayed

and applying the appropriate boundary conditions, reflection of the incident light from the structure can be obtained as $R = |\frac{F_{11}}{F_{12}}|^2$. Here, $F = \begin{bmatrix} F_{11} \\ F_{12} \end{bmatrix} = a_1^{-1} d_1 d_2^{-1} m_1 m_2^{-1} d_1 d_2^{-1} a_2$ where:

$$a_1 = \begin{bmatrix} 1 & 1 \\ \frac{ik_A}{\varepsilon_A} & \frac{-ik_A}{\varepsilon_A} \end{bmatrix}, a_2 = \begin{bmatrix} 1 \\ \frac{ik_A}{\varepsilon_A} \end{bmatrix} \tag{2.a}$$

$$d_1 = \begin{bmatrix} 1 & 1 \\ \frac{ik_D}{\varepsilon_D} & \frac{-ik_D}{\varepsilon_D} \end{bmatrix}, d_2 = \begin{bmatrix} e^{ik_D D_D} & e^{-ik_D D_D} \\ \frac{ik_D e^{ik_D D_D}}{\varepsilon_D} & \frac{-ik_D e^{-ik_D D_D}}{\varepsilon_D} \end{bmatrix} \tag{2.b}$$

$$m_1 = \begin{bmatrix} 1 & 1 \\ \frac{ik_M}{\varepsilon_M} & \frac{-ik_M}{\varepsilon_M} \end{bmatrix}, m_2 = \begin{bmatrix} e^{ik_M D_M} & e^{-ik_M D_M} \\ \frac{ik_M e^{ik_M D_M}}{\varepsilon_M} & \frac{-ik_M e^{-ik_M D_M}}{\varepsilon_M} \end{bmatrix} \tag{2.c}$$

and $k_{i=(A,D,M)} = \sqrt{\frac{\varepsilon_i \omega^2}{c^2} - k_x^2}$ where "c" is the speed of light. Moreover, D_D, D_M, and D_R are the thickness of the dielectric, middle material, and reflector layers, and ε_D and ε_M are permittivity of dielectric and metal, respectively. As illustrated in Fig. 1b, the proposed structure has Pt (with a thickness of 100 nm) as the back reflector material (i.e., thick bottom metal layer). It should be mentioned that in this section, our aim is to find the best middle layer and bottom layer is only a reflecting coating. Therefore, in all cases, in this part, the Pt layer is kept as bottom layer. Two identical Al_2O_3 layers with the same thickness of 80 nm have sandwiched the middle ideal metal layer. For each wavelength, the real and imaginary parts of permittivity of the ideal middle material are found in a way that the overall reflection from the stack is zero. Figure 1c illustrates the contour plot of the reflection (R) as a function of the real and imaginary parts of epsilon for a 10-nm-thick middle layer at the $\lambda = 1000$ nm. This plot clearly shows a group of centric circles around the zero reflection point (ZRP) where these circles radii get enlarged for larger values of R. Therefore, to be able to retain reflection below $R = 0.1$, the permittivity values (real and imaginary parts) for the middle layer should be located inside the $R = 0.1$ circle. To gain a better insight, the values for ZRPs of an ideal metal with thicknesses of $D_M = 5$ nm, 10 nm, 15 nm are plotted in Fig. 1d–f, respectively. The error bars are also utilized in these panels to define the range of values for the real and imaginary parts of permittivity where the reflection stays below 0.1 (more than 90% absorption). As these results illustrate, to have an ideal metal, the real part of the middle layer permittivity should take small values around zero (positive or negative) for $\lambda < 1000$ nm and this trend gradually grows toward positive values for longer wavelengths. This is actually the main reason that restricts the absorption capacity of metal-based multilayer designs since, for most of the metals, the real part of permittivity exponentially approaches large negative values as we move toward longer wavelengths. However, the imaginary part shows a relatively flatter response over the entire wavelength range except the shorter wavelengths ($\lambda < 600$ nm) where the values start to gradually grow from around zero to the flat response point. Moreover, comparing the extracted values for different metal thickness shows that the ZRPs are larger for thinner metal layers but at the same time the range of acceptable values for $R < 0.1$ is much wider. The situation is vice versa for thicker ideal metal layers. Therefore, to guarantee a reflection below 0.1, we need to choose our material in a way that its permittivity values are within the proposed range.

Some nonstoichiometric ceramic materials including transition metal carbides and nitrides show high carrier concentration and demonstrate an optical performance that is close to metals. However, in general, the real permittivity values for these dielectric materials are more close to zero (at the negative side). Therefore, it is expected that these materials can be an excellent option to replace metal–based multilayer absorbers. The comparison, on how well different metals, carbides, and nitrides are matched to this ideal model, is presented in Fig. 2a–c. The blue and red highlighted areas are the set of tolerable values for the real and imaginary parts of the permittivity of a 10-nm-thick ideal material that provide a reflection below $R < 0.1$. In this work, among other transition metal nitrides, VN and TiN are chosen to be explored. In the case of carbides, VC and TiC have been the choices of study. Figure 2a compares the permittivity values for Cr and Au with the ideal case. The permittivity values of Au and Cr have been obtained from CRC model. As it can be clearly seen, Au shows very poor agreement for both real and imaginary parts while permittivity values of Cr fairly meets the tolerable region for $\lambda < 1350$ nm . In fact, this mismatch is raised from the real part of the permittivity not that of its imaginary part. These findings from modeling are in agreement with what was obtained from the experimental results [48]. The results for the case of carbides and nitrides have been also depicted in Fig. 2b and c. The permittivity values for these four different materials have been taken from the works of Pflüger et al. [49, 50]. In the case of nitride-based materials, the real part of epsilon for VN crosses the border of the highlighted region in longer wavelengths compared to that of TiN. Furthermore, while the imaginary part is entirely inside the filled area for VN, it slightly stays out of the region for $\lambda < 750$ nm in the case of TiN. This matching is the best for the case of transition metal carbide materials. Figure 2c points out the real and imaginary parts of VC and TiC retained within the range up to 1380 nm. These results clearly elucidate the fact that transition metal

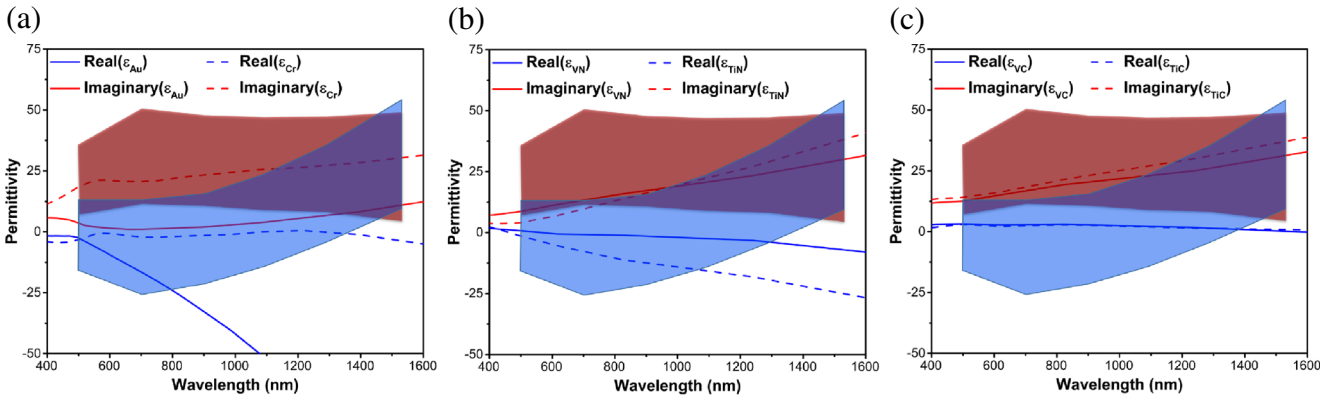

Fig. 2 Ideal permittivity region for perfect absorption. Comparison between real and imaginary parts of permittivity between **a** Au and Cr, **b** VN and TiN, and **c** VC and TiC and ideal case. The blue and red highlighted regions are tolerable real and imaginary values for $R < 0.1$, respectively

carbides and nitrides are excellent choices to put in the place of metals. In addition to their unprecedented optical behavior, these ceramic materials have superior thermal and chemical stability and they are refractory materials with an extremely high melting point that is a main factor to define the long-term stability of an absorber device. For example, Cr has a melting point of 1907 °C while this value for TiC is 3160 °C.

Structure and Simulation Setup

To evaluate our modeling results, we conducted numerical simulations to find the optimal configuration for each of the above materials. The role of different thicknesses in the overall absorption capability of the stack was scrutinized in the first step by employing numerical calculations using the commercial finite-difference time-domain (FDTD) software package (Lumerical FDTD Solutions). Throughout the simulations, the propagation direction of incident light was fixed to be perpendicular to the x–y plane. A broad plane wave with a linear x-polarized E field was being utilized to excite the unit cell and reflected (R) and transmitted (T) lights were recorded by two frequency domain power monitors on two sides of the multilayer structure. Periodic boundary conditions were also employed in the x and y directions, while boundaries in the z direction were adopted as a perfectly matched layer (PML). One-nanometer-sized mesh was added to the related simulation region in both the x- and y- directions. The refractive index data of the TMCs and TMNs is fittedusing the "Material Explorer" tool of the FDTD Solutions. Using fit tolerance as 0.0001 and max coefficients as 20, the materials were modeled closer to the material data in a better function. The simulations are performed with this fitted model.

The 2D view of planar MDMD array and 2D and 3D views of the designed trapezoidal MD pair array structure are illustrated in Figs. 1b and 3, respectively. They consist of alternating TMC (or TMN) and dielectric layers and TMC (or TMN) substrate. While planar configuration has two parameters, which are D_D and D_M, to be optimized, trapezoidal array configuration has four parameters, which are D_D, D_M, side-wall angle of the trapezoid design (α), and periodicity (P). Periodicity was kept at 250 nm and the geometries of the design were optimized by altering other parameters for each TMC, TMN, and metal. The main goal of this design is to cover the visible region and possible longest wavelength with near-unity absorption.

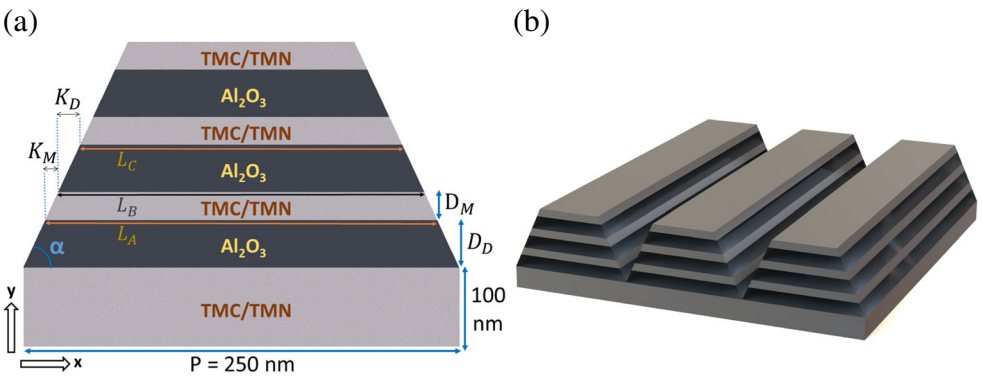

Fig. 3 Schematic illustration of the proposed trapezoidal MD pair array design **a** Unit cell of the structure in 2D. **b** Perspective view of the structure in 3D

The trapezoidal structure does not have a fine tip, but a tapered top layer. The width of the top layer is set by the side-wall angles, where the bottom width of the trapezoid is the same as the P. The side-wall angle can be calculated from the equation of $\alpha = \arctan\frac{D_M}{K_M} = \arctan\frac{D_D}{K_D}$, where K_M and K_D are the half of difference between bottom lengths of subsequent metallic and dielectric layers (L_A is bottom length of dielectric layer, L_B is bottom length of upper metal layer, and L_C is bottom length of upper dielectric layer), as shown in Fig. 3a. To be clear, if we call bottom and top width of a TMC/TMN layer as L_A and L_B, respectively, and top width of the upper dielectric layer as L_C, mathematically, $K_M = \frac{L_A - L_B}{2}$, $K_D = \frac{L_B - L_C}{2}$. K_M and K_D values are different to keep the side-wall angle constant since the thickness of the layers is different.

Absorption (A) was calculated using the equation of $A = 1 - R - T$. Considering the fact that the bottom reflecting layer thickness is much thicker than that of light skin depth at our operation frequencies, we can suppose T to be zero (this has been verified during our simulations). Consequently, the absorption can be found by the following simplified equation of $A \cong 1 - R$.

Results and Discussion

In planar MDMD configuration, we first optimized D_D in a way that the perfect absorption covers the whole visible range for all of the cases. In other words, its lower edge should be located at around 400 nm. During this optimization step, D_M was fixed at 10 nm. Taking $A = 0.9$ as the BW threshold, we can also define the upper edge of the regime. It should be noted that in all of the simulations the configuration has four layers. The bottom layer was chosen to be the same as the middle material coating with a thickness of 100 nm. Throughout this section, D_D-D_M-D_D annotation was employed to refer to a configuration of planar array (as an example, 75-10-75 means the dielectric layer thicknesses are 75 nm and the middle layer is 10 nm thick). Figure 4a–c show the results for VN absorbing layer. According to Fig. 4a, to ensure complete visible regime coverage, the thickness of the Al_2O_3 was fixed at 75 nm and to optimize the absorption BW and strength, thickness of the metal was swept from 6 nm to 16 nm, as shown in Fig. 4b. According to these panels, the largest BW belongs to 75-10-75 configuration covering from

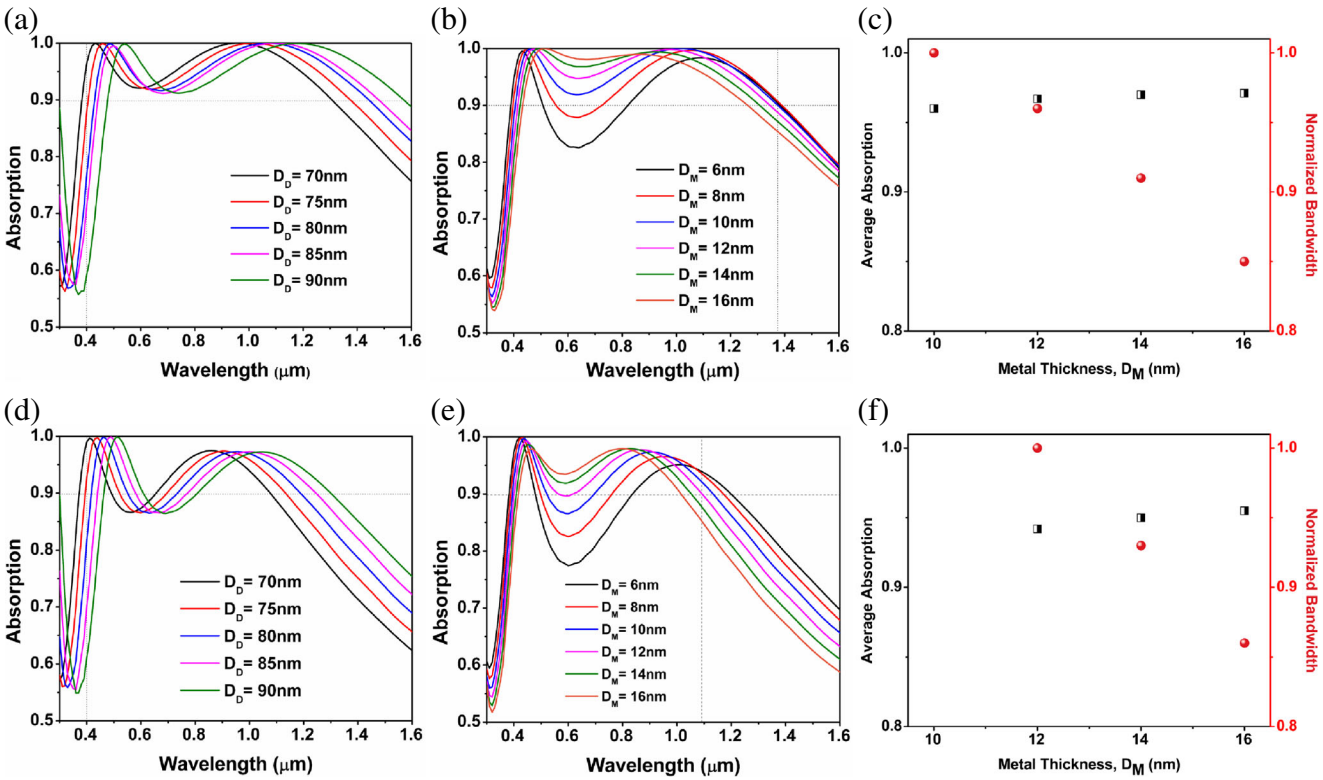

Fig. 4 Parameter optimization of nitride materials The impact of **a** dielectric thickness and **b** middle layer thickness in the absorption capability of the multilayer and **c** average light absorption and normalized BW for different material thickness in the case of VN multilayer. The impact of **d** dielectric thickness and **e** middle layer thickness in absorption response of the multilayer and **f** average absorption and normalized BW values for different TiN thickness

405 to 1375 nm with an overall BW of 970 nm. To have a better qualitative comparison, the normalized BW values for different metal thicknesses are presented in Fig. 4c. The BW of the multilayer is decreased to 0.85 moving from the metal thickness of 10 nm to 16 nm. In addition to this, the average absorption over the corresponding BW of each configuration is calculated and plotted in this figure. As it can be clearly seen, the average absorptions for all the cases are above 0.96 which proves a near-unity absorption from this configuration. The corresponding results for TiN case is also presented in Fig. 4d–f. Choosing the Al_2O_3 dielectric layer thickness (D_D) as 75 nm, the best performance was attained in the material thickness of $D_D = 12$ nm in which a BW of 695 nm can be accomplished (400 nm – 1095 nm). Using this number as a normalization factor, the BW drop trend for thicker layers was also depicted in Fig. 4f. For this material, the average absorption stays above 0.94 throughout its operation BW. These results are also in line with our findings discussed in the modeling section. For instance, based on our theoretical calculations, the imaginary part of TiN stays out of the $R < 0.1$ region for 500 nm $< \lambda <$ 800 nm. This can be confirmed by our numerical simulations where a dip in the absorption spectrum was observed in this wavelength range. Moreover, the fact that the absorption upper edge was located at longer wavelengths in the case of VN is also predicted by Fig. 2b. It is noteworthy that the theoretical findings have assumed an Al_2O_3 dielectric thickness of 80 nm while the results at Fig. 4 are found for optimal D_D thickness of 75 nm. The same systematic study was also carried out for carbide materials. The optical behavior for carbides is even better as shown in Fig. 5a–f. For the case of VC, in the optimal configuration of 75-10-75, the multilayer stack absorbs light over a broad wavelength regime of 415–1480 nm that corresponds to a BW of 1065 nm. Similar to VC, TiC has also superior light absorption capability, introducing absorption above 0.9 from 405 nm up to 1495 nm. In fact, the optimal multilayer configuration of 75-8-75 for TiC has the highest BW among all of the other choices with an average absorption above 0.95 throughout its BW, which is also wider than reported highest BW of metal-based MDMD designs, where a range from 400 to 1400 nm is absorbed utilizing the Cr-SiO_2 multilayer configuration [48].

To elucidate the mechanism of the absorption in this multilayer geometry, a contour plot displaying the amount

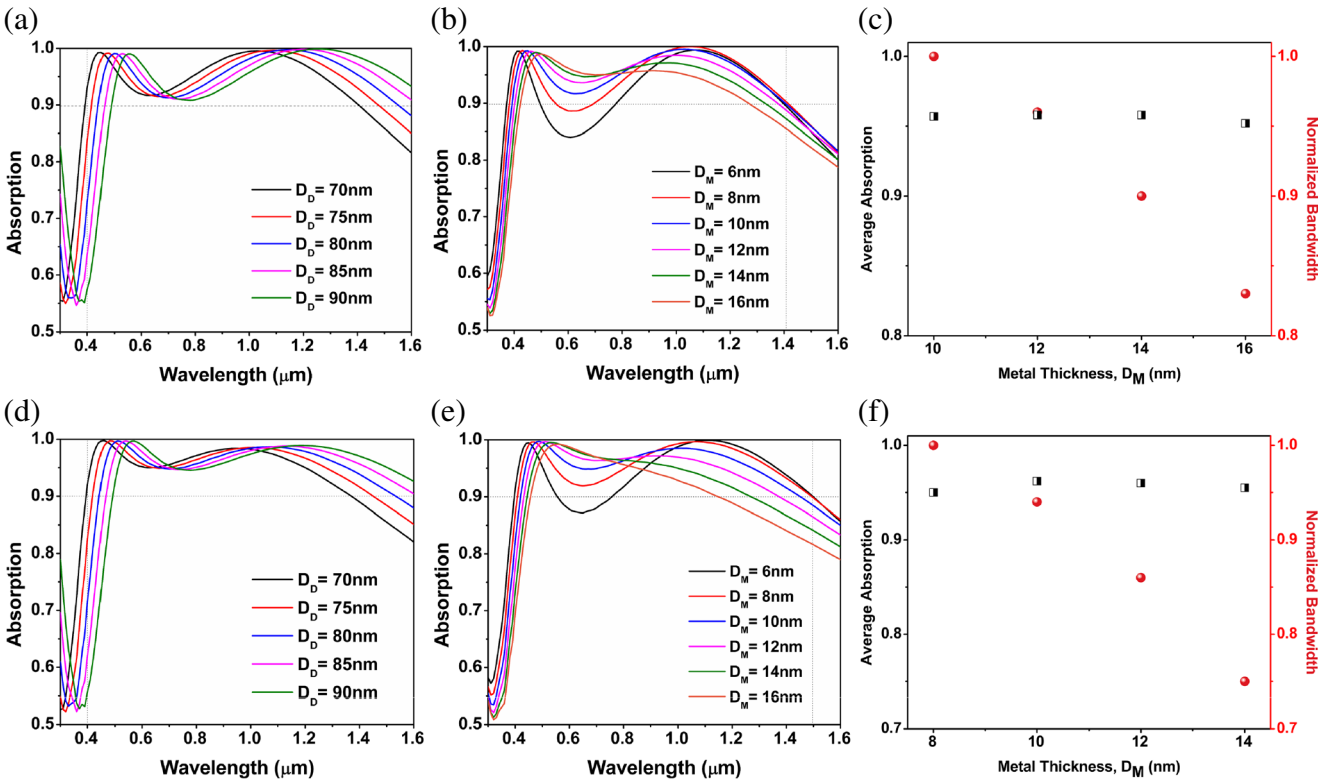

Fig. 5 Parameter optimization of nitride materials The impact of **a** dielectric thickness and **b** middle layer thickness in absorption capability of the multilayer and **c** average light absorption and normalized BW for different material thickness in the case of VC multilayer. The impact of **d** dielectric thickness and **e** middle layer thickness in absorption response of the multilayer and **f** average absorption and normalized BW values for different TiC thickness

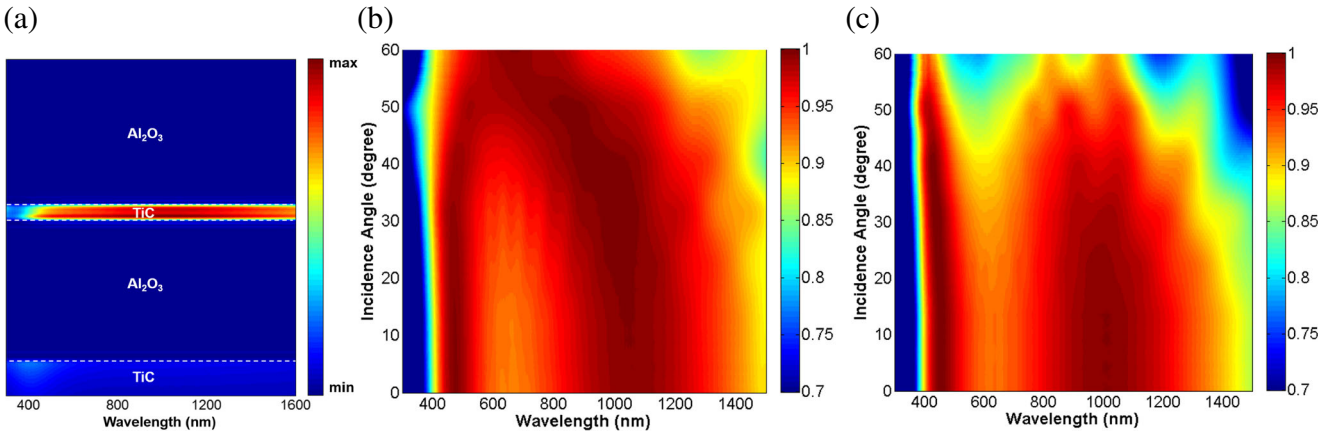

Fig. 6 Absorbed power and polarization dependency. **a** The contour plot comparing the absorbed power in different parts of MIMI design. The absorption values for **b** TM and **c** TE polarization for oblique incidence angles of $0° < \theta < 60°$

of absorbed light in different parts of a multilayer for the optimal case of TiC is plotted in Fig. 6a. As it can be clearly deduced from this panel, most of the light is concentrated in the middle absorbing layer. This is an expected result taking the high absorption coefficient of the nitride and carbide materials. Moreover, only a small portion of light in the lower wavelength values is absorbed using the bottom reflector layer. The oblique angle absorption response of the multilayer design is also plotted in Fig. 6b and c for transverse magnetic (TM) and transverse electric (TE) cases. As it is clearly illustrated in this figure, when the light is incident at longer angles, both the upper and lower edges of the absorption approach each other and, consequently, the absorption bandwidth get smaller. This case is more pronounced in the case of TE polarization incident light. However, in general, the absorber keeps its light absorption capability high over all oblique angles. This shows that this structure is not only an ultra-broadband absorber but also it shows a wide angle response over all incident angles.

Light absorption BW can be further extended utilizing larger number of MD pairs. Figure 7a–c depict the absorption spectra for MDMD and MDMDMD configurations for three optimal cases of VN, VC, and TiC. For both configurations, the thicknesses of layers are chosen as their optimal values found in the previous part. As Fig. 7a shows, the absorption BW can be extended to 1685 nm using a 3-pair multilayer architecture. An upper wavelength edge, as long as 1715 nm, can be obtained employing VC-based MDMDMD configuration, see Fig. 7b. BW extension is the largest for TiC where the absorption above 0.9 can be achieved in a wavelength range of 370–1895 nm (Fig. 7c). These findings reveal the capability of these materials to absorb light in an ultra-broadband regime where adding the number of pairs can extend the absorption BW toward longer wavelengths. However, a better approach to achieve broadest absorption response, while keeping the overall thickness the same, is to use tapered multilayer designs instead of planar ones. Therefore, a trapezoidal array structure comprised of 3 MD

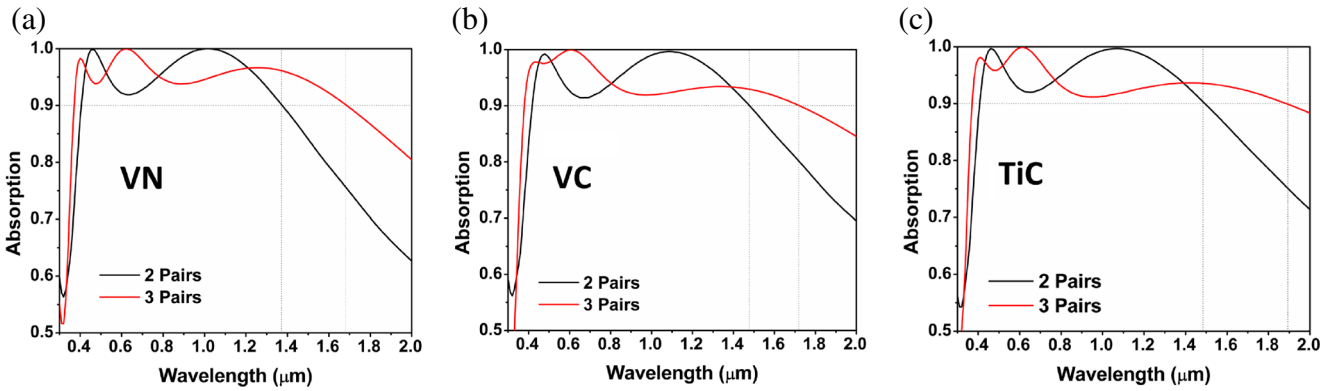

Fig. 7 BW improvement with increasing number of pairs. The absorption spectra of 2 pairs (MDMD) and 3 pairs (MDMDMD) configurations for the cases of **a** VN, **b** VC, and **c** TiC multilayers

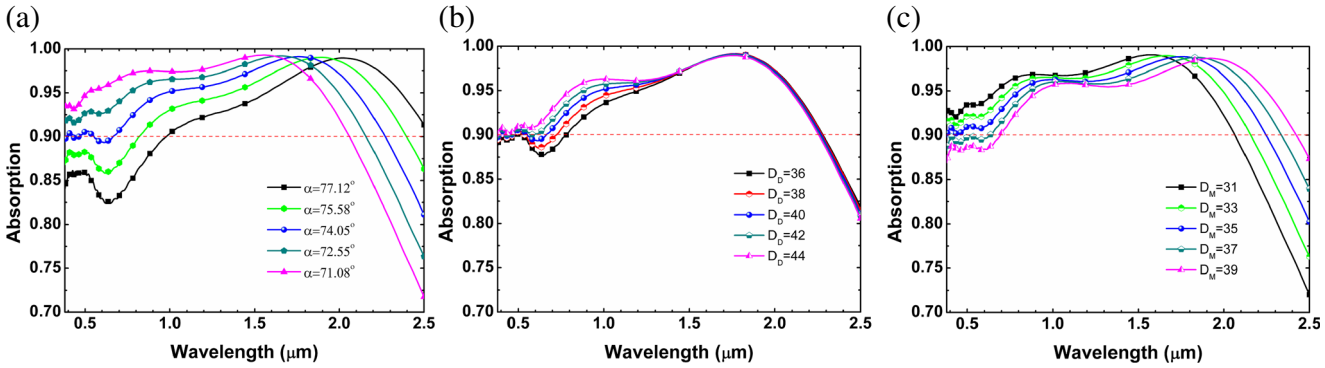

Fig. 8 Optimization process of TiC. **a** The impact of α when other parameters are $D_M = 35$ nm, $D_D = 40$ nm. **b** The impact of the thickness of the dielectric layer when other parameters are $D_M = 35$ nm, $\alpha = 74.05°$. **c** The impact of the thickness of TiC layer when other parameters are $D_D = 44$ nm, $\alpha = 74.05°$

pairs was designed and optimized for each TMC and TMN material to present higher performance of metal-free ultra-broadband perfect absorbers, and to reveal their superiority over commonly used metals.

In the MD pair–based trapezoidal array structure, we initially attained a good absorber using cursory parameters to understand the capability of the material in that geometrical shape. After the first set of results were obtained for each material, they were optimized in order to obtain the broadest absorption band. In all of the cases, we first optimized the side-wall angle of the trapezoid since a change in the optimal angle influences optimum values of the other parameters. Then, D_D was optimized considering that perfect absorption (above 0.9) is achieved in the visible region because D_D has a determining effect on the absorption at shorter wavelengths. Afterwards, D_M was optimized to have the broadest band. All of the structures were designed at the same period which is 250 nm. The designed structure for different materials was optimized in a way that its absorption spectrum fully covers the visible region and reaches to the possible longest wavelength. Figure 8a–c demonstrate the optimization process of the TiC. The first result is obtained when $D_M = 35$ nm, $D_D = 40$ nm, $\alpha = 74.05°$ and then α, D_D and D_M were optimized, respectively. According to Fig. 8a, side- wall angle of the trapezoid can be chosen either 74.05° or 72.55° since their results are above the 0.9 absorption. For $\alpha = 74.05°$, absorption decreases to below 0.9 at some wavelengths; however, it can be compensated with altering the thicknesses of the dielectric and TiC layers. Considering the purpose of having the largest BW, the $\alpha = 74.05°$ sidewall angle has better performance compared to the others. As shown in Fig. 8b, D_D has a significant effect on absorption at shorter wavelengths but it is insignificant at longer wavelengths. To ensure absorption is always higher than 0.9, this geometry is selected as 44 nm. It can be chosen as a higher value to increase absorption at the visible region; however, this brings about reduction on the BW. As shown in Fig. 8c, absorption stays above 0.9 and has the widest spectrum when $D_M = 35$ nm, which is the wavelength range of 380–2240 nm. Similar to TiC, the corresponding results for VC are shown in Fig. 9a–c. Its optimization

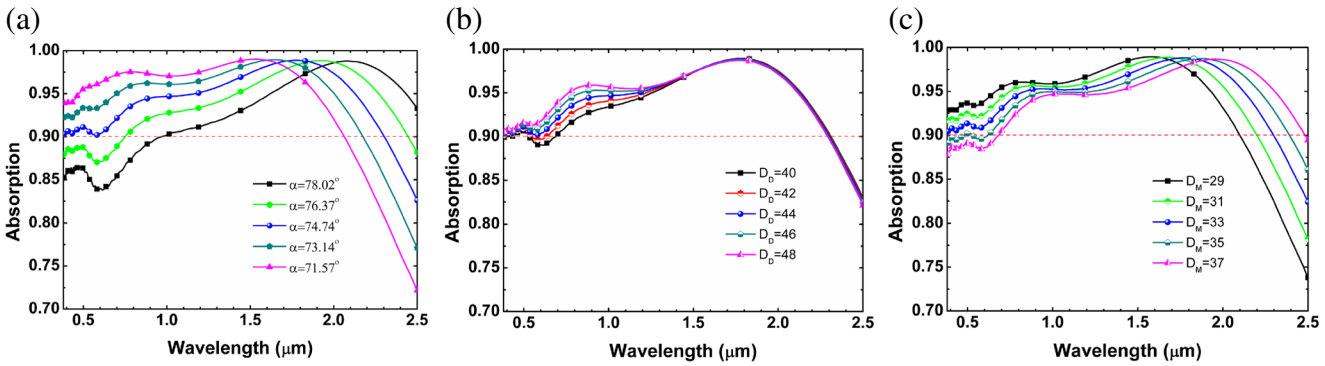

Fig. 9 Optimization process of VC. **a** The impact of α when other parameters are $D_M = 33$ nm, $D_D = 44$ nm. **b** The impact of the thickness of the dielectric layer when other parameters are $D_M = 33$ nm, $\alpha = 74.74°$. **c** The impact of the thickness of TiC layer when other parameters are $D_D = 44$ nm, $\alpha = 74.74°$

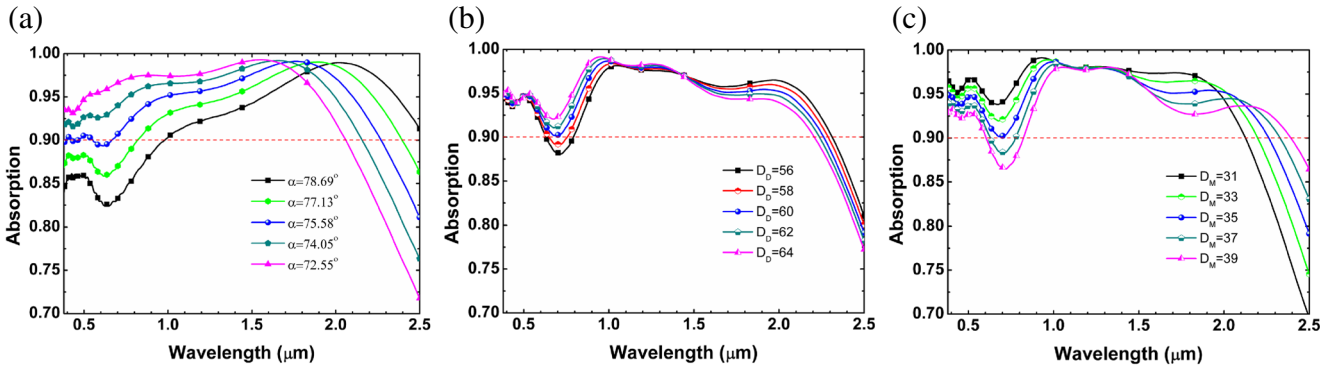

Fig. 10 Optimization process of TiN. **a** The impact of α when other parameters are $D_M = 35$ nm, $D_D = 60$ nm. **b** The impact of the thickness of the dielectric layer when other parameters are $D_M = 35$ nm, $\alpha = 75.58°$. **c** The impact of the thickness of TiC layer when other parameters are $D_D = 60$ nm, $\alpha = 75.58°$

process started with the parameters of $D_M = 33$ nm, $D_D = 44$ nm, $\alpha = 74.74°$. The values of α and D_D keep the absorption sufficiently high from 0.9 and $D_M = 33$ nm provides the broadest absorption spectrum. Therefore, the best performance is attained with these parameters in which absorption above 0.9 covers a range of 380–2290 nm. In the case of TiN, the optimization process is shown in Fig. 10a–c. The starting values were $D_M = 35$ nm, $D_D = 60$ nm, $\alpha = 75.58°$. Since absorption is not much below 0.9 at shorter wavelengths, α was not changed. To compensate for the dip that occurred around 700-nm wavelength, the dielectric thickness must be increased sufficiently. $D_D = 60$ nm is enough to keep absorption a little higher than 0.9. It can be increased to guarantee that it does not fall below 0.9; however, we kept it as 60 nm for the sake of broadest BW. Then, absorption above 0.9 in the wavelength range of 380–2265 nm is attained when $D_M = 35$ nm. As demonstrated in Fig. 11a–c, VN performs superior light absorption than other TMC&TMN materials. For parameters of $D_M = 36$ nm, $D_D = 50$ nm, $\alpha = 75.96°$, the designed structure has absorptivity above 0.9 in the wavelength range of 380–2500 nm, even more (we could not simulate longer wavelengths since we do not have refractive index data of the materials). Although VN is not a commonly used material, it is the only one that has such a performance with this design.

As the best performances of TMC&TMN materials are compared in Fig. 12a, VN shows the best performance (i.e., the broadest BW) in the trapezoidal array configuration among TMCs&TMNs. Furthermore, the type of the dielectric used in the design can also affect the absorption spectrum. Simulations were repeated replacing Al_2O_3 with SiO_2 and TiO_2 and results are plotted in Fig. 12b when VN is used. TiO_2 has more absorption strength and can have a longer spectrum if data of the materials would be available. Nevertheless, all three of them satisfy the valid wavelength range, which is 380–2500 nm.

To have a comprehensive study on the potential of these ceramic materials in the absorber design, the performance of the commonly used metals and VN should be compared. VN has higher melting point and resistance to oxidation and erosion compared to metals; however, its optical performance also has a crucial importance. Similar simulations were repeated to find the optimal geometries

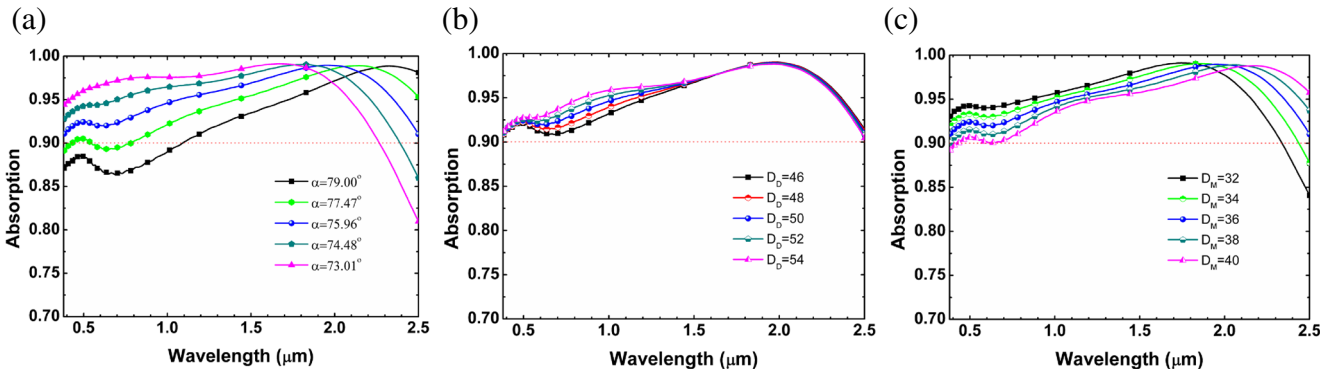

Fig. 11 Optimization process of VN. **a** The impact of α when other parameters are $D_M = 36$ nm, $D_D = 50$ nm. **b** The impact of the thickness of the dielectric layer when other parameters are $D_M = 36$ nm, $\alpha = 75.96°$. **c** The impact of the thickness of TiC layer when other parameters are $D_D = 50$ nm, $\alpha = 75.96°$

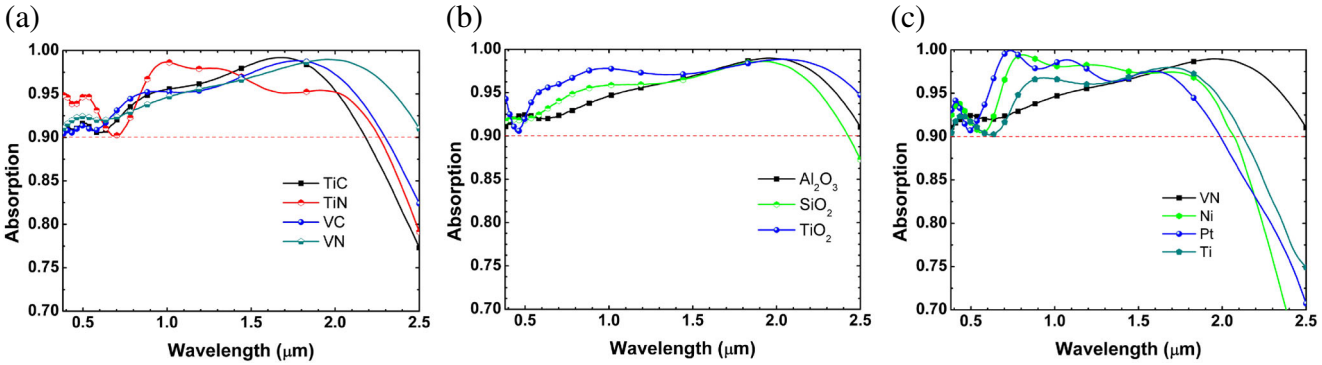

Fig. 12 Comparison of the best performances of TMCs,TMNs and metals. **a** Comparison of the largest absorption spectrum attained with TMC (TiC, VC) and TMN (TiN, VN) materials. **b** The impact of the dielectric layer type on absorption when VN is used. **c** Comparison of the best performances of VN, Ti, Pt, and Ni

for each metal in trapezoidal array structure. As a result, while the optimal configuration of Ni with parameters of $D_M = 32$ nm, $D_D = 54$ nm, $\alpha = 72.65°$ exhibits an absorption above 0.9 between 380 and 2070 nm, Pt with best parameters for the optimum absorption $D_M = 32$ nm, $D_D = 50$ nm, $\alpha = 71.03°$ performs perfect absorption between 380 and 1990 nm and optimized Ti structure with parameters of $D_M = 33$ nm, $D_D = 52$ nm, $\alpha = 74.75°$ shows perfect absorption in the wavelength range of 380–2125 nm. Therefore, VN performs better absorptivity than all lossy metals, as presented in Fig. 12c, besides being more durable to temperature and oxidation. That makes it a perfect candidate for high-temperature broadband perfect absorber applications.

In order to understand how and where electromagnetic waves are absorbed by the designed perfect absorber, we examined the electric and magnetic field distributions at several wavelengths throughout the absorption spectrum. Electric fields are mainly localized at the edges of metallic and dielectric layers and in the air gaps around metal, as shown in Fig. 13a–c. While the electric field is mostly localized near the top of the trapezoid at 684-nm

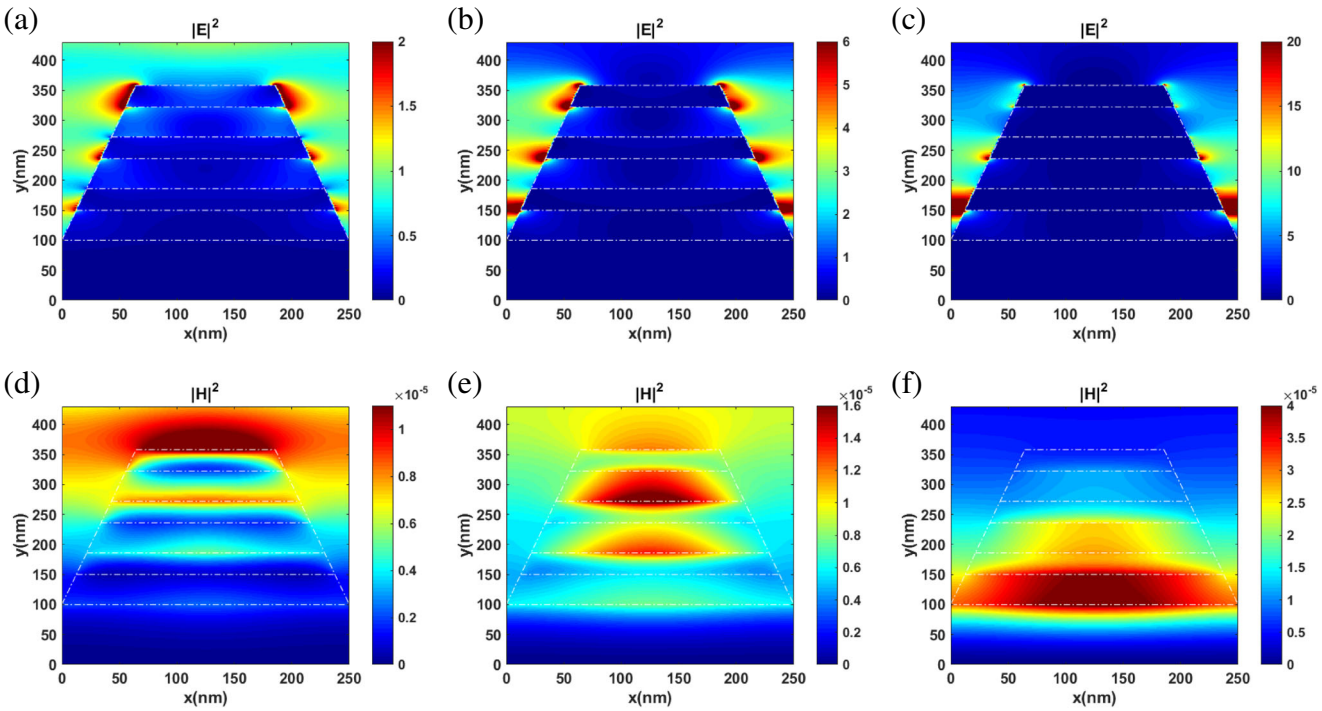

Fig. 13 Electric and magnetic field distributions. Magnitude square of E field distribution when **a** wavelength is 684 nm, **b** wavelength is 1350 nm, **c** wavelength is 2500 nm. Magnitude square of H field distribution when **d** wavelength is 684 nm, **e** wavelength is 1350 nm, **f** wavelength is 2500 nm

wavelength, it is concentrated at each metal-dielectric cross-section and increased toward the bottom at 1350 nm, and it is mostly localized at the bottom of the trapezoid in the air gap when the wavelength is 2500 nm. As it is inferred from Fig. 13a–c, electric field strength is improved with longer wavelengths and the localization region moves toward the bottom of the trapezoid. Contrary to the electric field, the magnetic field is localized between metallic layers, namely inside the dielectric, as shown in Fig. 13d–f. When the wavelength is 684 nm, the magnetic field is mainly localized in the air (just above the top metallic layer) and a part of it is localized at the boundary of dielectric and metal in the middle. Figure 13e and f demonstrate that the magnetic field is localized inside the structure in dielectrics as the wavelength becomes longer. Similar to the electric field, the magnetic field gets stronger and localized near the bottom of the structure as the wavelength becomes longer. Therefore, in this tapered design, in every wavelength range, the active region of the absorber changes. The superposition of these responses leads to such ultra-broadband light perfect absorption. We can deduce here that if the number of VN-Al_2O_3 pairs is increased, this structure can absorb even longer wavelengths.

Fabrication Considerations

Another important feature that should be considered in this design is its fabrication considerations. In this part, we will present some possible fabrication errors, their effects on the results, and alternative solutions to compensate their negative effects and to obtain the same performance as mentioned before.

The first possible problem is difficulties in achieving adjacent trapezoids (with zero spacing) in a periodic fashion. The existence of a space may be unavoidable depending on the fabrication route used. The modified structure considering this factor and the resulting absorption spectrum are shown in Fig. 14a and b. Longer wavelengths cannot be absorbed perfectly anymore and absorption BW gets significantly narrower. This is due to the fact that a part of the incident light fully reflects from these spacing regions. To compensate for the disadvantage of fabrication feasibilities, we proposed a new design to replace the substrate with an MDM design which is composed of the same dielectric and material (VN), as shown in Fig. 14c. The MDM layer was designed for the case when 50-nm space is left between the adjacent trapezoids. The optimization

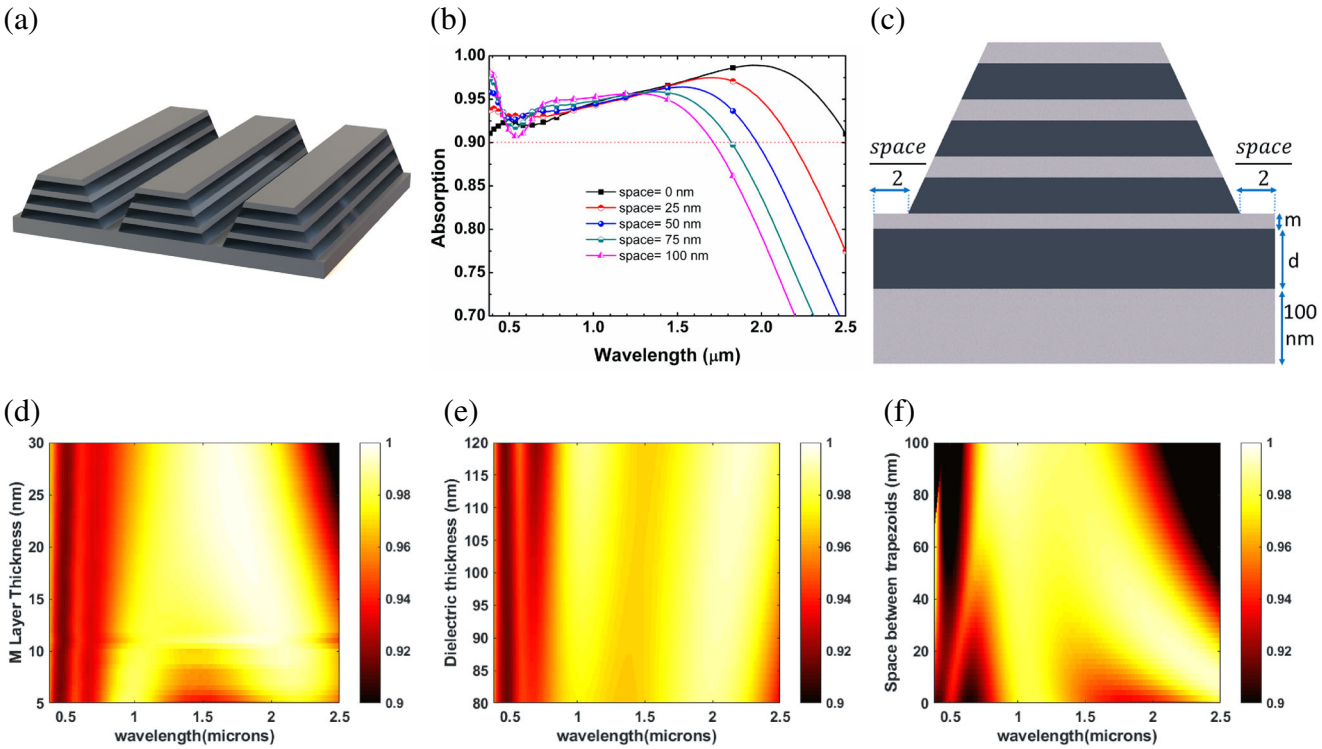

Fig. 14 Possible problems encountered in fabrication. **a** The new 3D view of the structure if space is left between trapezoids. **b** Resulting absorption spectrum if space is left between trapezoids. **c** Proposed new design to compensate fabrication error and obtain the same result as before. **d** Optimization of m. **e** Optimization of d. **f** Absorption spectrum while space left between trapezoids is changed from 0 to 100 nm when the designed MDM is present under the trapezoidal structure

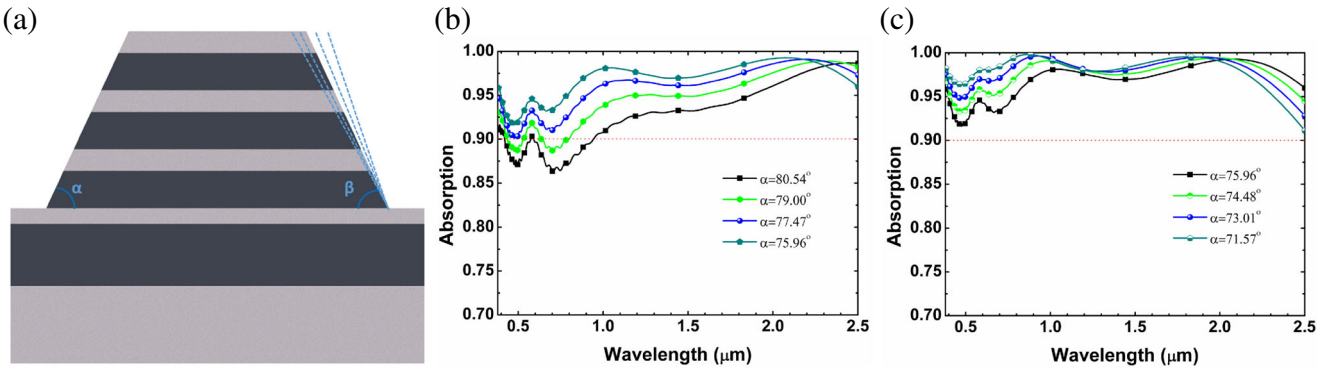

Fig. 15 Effect of side-wall angle error on absorption spectrum **a** 2D view of the structure if one side wall is not fabricated correctly. **b** Absorption spectrum if one side wall is steeper than expected. **c** Absorption spectrum if one side wall is less steep than expected

process of geometries of the MDM structure is shown in Fig. 14d and e. The bottom thick VN layer was chosen as 100 nm and the dielectric and thin VN layers were optimized one by one. At first, the dielectric layer was fixed to 100 nm and the thickness of the upper layer was swept from 5 to 30 nm. As shown in Fig. 14d, many of them result in absorption above 0.9, so we chose 10 nm to have the largest BW and tolerance to fabrication errors. Then, VN thickness was fixed to 10 nm and the dielectric thickness was swept from 80 to 120 nm. As shown in Fig. 14e, all of them again satisfy the requirements. Increasing the dielectric thickness gives a rise in absorption in longer wavelengths, however, causes fall in shorter wavelengths. To have a tolerance in both ways, we chose a 100-nm-thick dielectric layer. The resulting absorption spectrum of the design for different spaces between trapezoids is demonstrated in Fig. 14f. Thus, if the fabrication of designed ceramic-based trapezoidal array does not function as simulated due to fabrication limitations, adding a simple MDM layer increases its performance back into the desired levels or even better.

Side-wall angles of the trapezoid are hard to fabricate exactly as expected. Having tolerance for that is a precious property. We examined the effects of fabricating different side-wall angles on the absorption strength and spectrum. One of the side walls was drawn as planned in the optimal configuration, which is $\alpha = 75.96°$ for VN, and the angle of the other wall was selected as higher and smaller values. In other words, the symmetric design of the trapezoids was distorted to an asymmetric one. The primitive shape of this error is shown in Fig. 15a. When one wall becomes steeper than optimal configuration, problems with shorter wavelengths occur, as shown in Fig. 15b. While the absorption strength is increased in the NIR region, it decreases below 0.9 in the visible region. When one side-wall angle becomes less than expected, while absorption in the visible region is increased, absorption at longer wavelengths decreases but still stays above 0.9, as shown in Fig. 15c. Therefore, the side-wall angle has 2° tolerance for bigger angles and 4° tolerance for smaller angles when one wall is produced as planned. Even if the angle is distorted more, bigger or smaller, in both cases, the absorption stays above 0.85.

Conclusion

In this paper, we demonstrated unprecedented potentials of transition metal carbides and nitrides to design perfect light absorbers in ultra-broadband range, and indicated that these materials perform perfect electromagnetic wave absorption in a larger bandwidth than metals in any configuration, owing to their excellent optical properties. Our numerical findings show that the proposed ceramic materials have wider bandwidth than all lossy and plasmonic materials in both planar metal-dielectric-metal-dielectric configuration and trapezoidal array of metal-dielectric pairs. In planar configuration, titanium carbide exhibits the largest bandwidth where an absorption above 0.9 is observed in the range of 405–1495 nm. Using the trapezoidal array structure, the best performance is observed for vanadium nitride where an absorption above 0.9 is retained over the range of 300–2500 nm. In addition, we investigated the effects of possible fabrication inaccuracies in fabricating the trapezoidal array structure, and we proposed an alternative design to preserve the same performance. The superior absorption performance of transition metal carbides and nitrides over metals along with their higher durability against temperature, oxidation, and erosion make them highly promising in ultra-broadband perfect absorber applicat ions in which thermal requirements are strict in addition to high optical performance.

Authors' Contributions First Author (M.C.S.) carried out the modeling, design, and simulations. A.G. assisted in the modeling and design and D.U.Y. assisted in theoretical review and simulations. E.O. and V.B.E. supervised the study. All the authors contributed in the results, discussions, and paper writing.

Funding Authors reveived financial support from the Scientific and Technological Research Council of Turkey (TUBITAK) and DPT-HAMIT under the Project nos. 113E331, 114E374, and 115F560. One of the authors (E.O.) also received partial financial support from the Turkish Academy of Sciences (TUBA)

References

1. Luo S, Zhao J, Zuo D, Wang X (2016) Opt Express 24(9):9288. https://doi.org/10.1364/OE.24.009288. https://www.osapublishing.org/abstract.cfm?URI=oe-24-9-9288
2. Li Y, Su L, Shou C, Yu C, Deng J, Fang Y (2013) Sci Rep 3. https://doi.org/10.1038/srep02865
3. Rephaeli E, Fan S (2009) Opt Express 17(17):15145. https://doi.org/10.1364/OE.17.015145. https://www.osapublishing.org/oe/abstract.cfm?uri=oe-17-17-15145
4. Wu C, Neuner B, John J, Milder A, Zollars B, Savoy S, Shvets G (2012) J Opt 14(2). https://doi.org/10.1088/2040-8978/14/2/024005
5. Li W, Valentine J (2014) Nano Lett 14(6):3510. https://doi.org/10.1021/nl501090w
6. Liu N, Mesch M, Weiss T, Hentschel M, Giessen H (2010) Nano Lett 10(7):2342. https://doi.org/10.1021/nl9041033
7. Ding F, Dai J, Chen Y, Zhu J, Jin Y, Bozhevolnyi SI (2016) Sci Rep 6. https://doi.org/10.1038/srep39445
8. Hendrickson J, Guo J, Zhang B, Buchwald W, Soref R (2012) Opt Lett 37(3):371. https://doi.org/10.1364/OL.37.000371. https://www.osapublishing.org/abstract.cfm?URI=ol-37-3-371
9. Bouchon P, Koechlin C, Pardo F, Haïdar R., Pelouard JL (2012) Opt Lett 37(6):1038. https://doi.org/10.1364/OL.37.001038. https://www.osapublishing.org/abstract.cfm?URI=ol-37-6-1038
10. Hao J, Wang J, Liu X, Padilla WJ, Zhou L, Qiu M (2010) Appl Phys Lett 96(25). https://doi.org/10.1063/1.3442904
11. Wang H, Wang L (2013) Opt Express 21(S6):A1078. https://doi.org/10.1364/OE.21.0A1078. https://www.osapublishing.org/oe/abstract.cfm?uri=oe-21-S6-A1078
12. Wu C, Shvets G (2012) Opt Lett 37(3):308. https://doi.org/10.1364/OL.37.000308. https://www.osapublishing.org/abstract.cfm?URI=ol-37-3-308
13. Zhang B, Hendrickson J, Guo J (2013) J Opt Soc Am B 30(3):656. https://doi.org/10.1364/JOSAB.30.000656. https://www.osapublishing.org/abstract.cfm?URI=josab-30-3-656
14. Ghobadi A, Hajian H, Butun B, Ozbay E (2018) Strong light-matter interaction in lithography-free planar metamaterial perfect absorbers. https://doi.org/10.1021/acsphotonics.8b00872
15. Ghobadi A, Hajian H, Gokbayrak M, Abedini Dereshgi S, Toprak A, Butun B, Ozbay E (2017) Opt Express 25(22):20256. https://doi.org/10.1364/OE.25.027624
16. Aydin K, Ferry VE, Briggs RM, Atwater HA (2011) Nat Commun 2(1). https://doi.org/10.1038/ncomms1528
17. Wang J, Chen Y, Hao J, Yan M, Qiu M (2011) J Appl Phys 109. https://doi.org/10.1063/1.3573495
18. Feng Q, Pu M, Hu C, Luo X (2012) Opt Lett 37(11):2133. https://doi.org/10.1364/OL.37.002133. https://www.osapublishing.org/abstract.cfm?URI=ol-37-11-2133
19. Zhang Y, Zhou L, Li JQ, Wang QJ, Huang CP (2015) Sci Rep 5. https://doi.org/10.1038/srep10119
20. Guo W, Liu Y, Han T (2016) Opt Express 24(18):20586. https://doi.org/10.1364/OE.24.020586. https://www.osapublishing.org/abstract.cfm?URI=oe-24-18-20586
21. Nielsen MG, Pors A, Albrektsen O, Bozhevolnyi SI (2012) Opt Express 20(12):13311. https://doi.org/10.1364/OE.20.013311. https://www.osapublishing.org/oe/abstract.cfm?uri=oe-20-12-13311
22. Hu D, Wang H, Zhu QF (2016) J Nanophotonics 10(2):026021. https://doi.org/10.1117/1.JNP.10.026021. http://nanophotonics.spiedigitallibrary.org/article.aspx?doi=10.1117/1.JNP.10.026021
23. Shen S, Qiao W, Ye Y, Zhou Y, Chen L (2015) Opt Express 23(2):963. https://doi.org/10.1364/OE.23.000963
24. Mattiucci N, Bloemer MJ, Aközbek N, D'aguanno G (2013) Sci Rep 3. https://doi.org/10.1038/srep03203
25. Ghobadi A, Hajian H, Dereshgi SA, Bozok B, Butun B, Ozbay E (2017) Sci Rep 7(1). https://doi.org/10.1038/s41598-017-15312-w
26. Ghobadi A, Dereshgi SA, Hajian H, Bozok B, Butun B, Ozbay E (2017) Sci Rep 7(1). https://doi.org/10.1038/s41598-017-04964-3
27. Abedini Dereshgi S, Ghobadi A, Hajian H, Butun B, Ozbay E (2017) Sci Rep 7(1). https://doi.org/10.1038/s41598-017-13837-8
28. Ghobadi A, Hajian H, Rashed AR, Butun B, Ozbay E (2018) Photonics Res. https://doi.org/10.1364/PRJ.6.000168
29. Lei JG, Ji BY, Lin JQ (2016) Chin J Phys 54(6):940. https://doi.org/10.1016/j.cjph.2016.09.003
30. Cui Y, Fung KH, Xu J, Ma H, Jin Y, He S, Fang NX (2012) Nano Lett 12(3):1443. https://doi.org/10.1021/nl204118h
31. Liang Q, Wang T, Lu Z, Sun Q, Fu Y, Yu W (2013) Adv Opt Mater 1(1):43. https://doi.org/10.1002/adom.201200009
32. Ji D, Song H, Zeng X, Hu H, Liu K, Zhang N, Gan Q (2014) Sci Rep 4. https://doi.org/10.1038/srep04498
33. He S, Ding F, Mo L, Bao F (2014) Prog Electromagn Res 147(May):69. https://doi.org/10.2528/PIER14040306. http://www.jpier.org/PIER/pier.php?paper=14040306
34. Ding F, Jin Y, Li B, Cheng H, Mo L, He S (2014) Laser Photonics Rev 8(6):946. https://doi.org/10.1002/lpor.201400157
35. Zhong YK, Fu SM, Ju NP, Tu MH, Chen BR, Lin A (2016), IEEE Photon J 8(1). https://doi.org/10.1109/JPHOT.2015.2507368
36. Wang J, Zhang W, Zhu M, Yi K, Shao J (2015) Plasmonics 10(6):1473. https://doi.org/10.1007/s11468-015-9962-x
37. Naik GV, Schroeder JL, Sands TD, Boltasseva A (2010) Opt Mater Express 2(4):478. https://doi.org/10.1364/OME.2.000478
38. Cortie MB, Giddings J, Dowd A (2010) Nanotechnology 21(11). https://doi.org/10.1088/0957-4484/21/11/115201
39. Naik GV, Kim J, Boltasseva A (2011) Opt Mater Express 1(6):1090. https://doi.org/10.1364/OME.1.001090. https://www.osapublishing.org/ome/abstract.cfm?uri=ome-1-6-1090
40. Li W, Guler U, Kinsey N, Naik GV, Boltasseva A, Guan J, Shalaev VM, Kildishev AV (2014) Adv Mater 26(47):7959. https://doi.org/10.1002/adma.201401874
41. Chen F, Li Q, Li M, Long H, Yao Y, Sun P, Zhang J (2016) 16th international conference on numerical simulation of optoelectronic devices. In: NUSOD, vol 2016, pp 111–112. https://doi.org/10.1109/NUSOD.2016.7547055
42. Wang H, Chen Q, Wen L, Song S, Hu X, Xu G (2015) Photon Res 3(6):329. https://doi.org/10.1364/PRJ.3.000329. https://www.osapublishing.org/abstract.cfm?URI=prj-3-6-329
43. Chaudhuri K, Alhabeb M, Wang Z, Shalaev VM, Gogotsi Y, Boltasseva A (2018) ACS Photon 5(3):1115. https://doi.org/10.1021/acsphotonics.7b01439
44. Alhabeb M, Maleski K, Mathis TS, Sarycheva A, Hatter CB, Uzun S, Levitt A, Gogotsi Y (2018) Angew Chem Int Ed 57(19):5444. https://doi.org/10.1002/anie.201802232

45. Hantanasirisakul K, Gogotsi Y (2018) Adv Mater 1804779: 1804779. https://doi.org/10.1002/adma.201804779. http://doi.wiley.com/10.1002/adma.201804779
46. Chaudhuri K, Shaltout A, Shah D, Guler U, Dutta A, Shalaev VM, Boltasseva A (2018) ACS Photonics p. acsphotonics.8b00943. https://doi.org/10.1021/acsphotonics.8b00943. http://pubs.acs.org/doi/10.1021/acsphotonics.8b00943
47. Wang Z, Shah D, Chaudhuri K, Catellani A, Alhabeb M, Reddy H, Meng X, Azzam SI (2018) In: 2018 12th international congress on artificial materials for novel wave phenomena (metamaterials), IEEE, pp 001, pp 58–60. https://doi.org/10.1109/MetaMaterials.2018.8534052
48. Deng H, Li Z, Stan L, Rosenmann D, Czaplewski D, Gao J, Yang X (2015) Opt Lett 40(11):2592. https://doi.org/10.1364/OL.40.002592. https://www.osapublishing.org/abstract.cfm?URI=ol-40-11-2592
49. Pflüger J, Fink J, Weber W, Bohnen KP, Crecelius G (1984) Phys Rev B 30(3):1155. https://doi.org/10.1103/PhysRevB.30.1155
50. Pflüger J, Fink J (1997) In: Handbook of optical constants of solids. https://doi.org/10.1016/B978-012544415-6.50055-8